Engineering Fracture Mechanics 96 (2012) 401–415

Contents lists available at SciVerse ScienceDirect

Engineering Fracture Mechanics

journal homepage: www.elsevier.com/locate/engfracmech

Determination of fracture toughness of AZ31 Mg alloy using the cohesive finite element method

X. Guo [a,b,*], K. Chang [c], L.Q. Chen [c], M. Zhou [d,*]

[a] School of Mechanical Engineering, Tianjin University, Tianjin 300072, China
[b] Tianjin Key Laboratory of Nonlinear Dynamics and Chaos Control, Tianjin 300072, China
[c] Department of Materials Science and Engineering, The Pennsylvania State University, University Park, PA 16802, USA
[d] The George W. Woodruff School of Mechanical Engineering, Georgia Institute of Technology, Atlanta, GA 30332-0405, USA

ARTICLE INFO

Article history:
Received 24 January 2012
Received in revised form 21 June 2012
Accepted 11 August 2012

Keywords:
Fracture toughness
Cohesive finite element method
Microstructure
Plasticity
Mg alloy

ABSTRACT

The objective of this study is to develop a micromechanical approach for determining the fracture toughness. A phase-field model for grain growth is employed to generate microstructures with varying attributes and the cohesive finite element method is employed to quantify the interaction between a propagating crack and microstructures of an AZ31 Mg alloy. Simulations show that fracture toughness increases as the average grain size decreases and that the local crack tip environment significantly affects the fracture behavior. Dramatically different dependences of fracture toughness on overall strain rate are seen when two different types of cohesive laws are employed.

1. Introduction

Metallic alloys are microscopically-heterogeneous materials widely used in engineering. Among different metallic alloys, Mg alloys have been of recent interest due to increasing demand for light-weight materials in industry. The AZ31 Mg alloy has attractive mechanical properties, including high specific strength, good tensile properties [1], high machinability, and fatigue resistance [2]. Since AZ31 is not as tough as widely-used Al alloys, much effort has been devoted to investigating and improving its fracture resistance. Somekawa and Mukai [3,4] found that AZ31 Mg alloy samples with a pre-crack normal to the basal plane have a higher fracture toughness than those with a pre-crack parallel to the basal plane. Somekawa and Mukai [5] improved the fracture toughness of the AZ31 Mg alloy by refining grain structure in an equal-channel-angular-extrusion (ECAE) process.

Designing microstructures for improving fracture resistance requires a detailed understanding of how an advancing crack interacts with the microstructures at multiple length scales [6]. Microscale failure can be analyzed by explicit micromechanical simulations. Through the consideration of representative samples of actual microstructures, effects of various fracture mechanisms can be delineated. The required features of the simulation framework should include (1) explicit accounting of real, arbitrary material microstructures, and (2) explicit modeling of fracture in a non-constrained manner so that arbitrary crack paths or microcrack patterns are admitted.

Among the multiple approaches for investigating fracture, the cohesive finite element method (CFEM) and the eXtended finite element method (XFEM) have shown their effectiveness. Song et al. [7] studied their performances for analyzing

* Corresponding authors. Address: School of Mechanical Engineering, Tianjin University, Tianjin 300072, China. Tel.: +86 22 2740 4934; fax: +86 22 8740 1979 (X. Guo), tel.: +1 404 894 3294; fax: +1 404 894 8336 (M. Zhou).
E-mail addresses: xiangguo@tju.edu.cn (X. Guo), min.zhou@gatech.edu (M. Zhou).

0013-7944/$ - see front matter © 2012 Elsevier Ltd. All rights reserved.
http://dx.doi.org/10.1016/j.engfracmech.2012.08.014

Nomenclature

a	half length of central crack
B	thickness of CCT specimen
C	strain-rate sensitivity parameter
D	damage parameter for cohesive separation
$\mathbf{D}$	total rate of deformation
$\mathbf{D}^e$	elastic part of the rate of deformation
$\mathbf{D}^p$	plastic part of the rate of deformation
f_0	local free energy density in phase-field simulation
F	total free energy of the system in phase-field simulation
G_F	fracture energy
K	stress intensity factor
K_{IC}	fracture toughness
$\mathbf{L}$	tensor of isotropic elastic moduli
M_i	grain boundary mobilities
P	load at the upper or lower boundary of the CCT specimen
T	effective traction
T_m	cohesive strength
T_n	cohesive traction in the normal direction
T_t	cohesive traction in the tangential direction
w	effective separation
w_c	critical separation beyond which the traction becomes zero for the homogenized alloy, the grain interior, the grain boundary-affected zone, and the interface
w_m	characteristic separation at which T reaches T_m
w_n	normal separation across the cohesive surfaces
w_t	tangential separation across the cohesive surfaces
W	half width of the CCT specimen
α, β, γ	phenomenological constants in local free energy density function f_0
δ	opening displacement of the pre-crack tip
δ_{cr}	critical crack tip opening displacement
Δt	time step size in phase-field simulation
Δx	grid spacing in phase-field simulation
$\dot{\varepsilon}$	strain rate
$\dot{\varepsilon}_0$	reference strain rate
$\bar{\varepsilon}_p$	equivalent plastic strain
$\dot{\bar{\varepsilon}}_p$	effective plastic strain rate
$\eta_1, \eta_2, \ldots, \eta_Q$	a set of order parameters in phase-field simulation
κ_i	gradient energy coefficients in phase-field simulation
σ_0	yield stress under quasi-static conditions
$\bar{\sigma}$	von Mises stress
$\sigma(\dot{\varepsilon}_0)$	reference stress–strain curve at the reference strain rate
$\hat{\tau}$	Jaumann rate of Kirchhoff stress
τ'	devitoric stress
APT	active parameter tracking
CCT	center-cracked-tension
CFEM	cohesive finite element method
CTOD	crack tip opening displacement
ECAE	equal-channel-angular-extrusion
FPZ	fracture process zone
GBAZ	grain boundary-affected zone
GI	grain interior
HA	homogenized alloy
XFEM	eXtended finite element method

dynamic crack propagation in brittle materials. They found that the XFEM and the CFEM showed similar crack speeds and crack paths. In contrast, the element deletion method performed very poorly and was unable to predict crack branching. They also pointed out that current difficulty with the XFEM lied in the modeling of spontaneous multiple crack initiation, branching, and coalescence. Our research in this study concentrates on both the propagation of a pre-crack and the nucleation and the propagation of multiple microcracks around the pre-crack tip within the fracture process zone (FPZ). Therefore, the CFEM is an appealing approach for our research.

The CFEM has been developed since the 1980s [8,9]. It incorporates the concept of cohesive surface into the finite element model, allowing fracture processes to be modeled explicitly. A large amount of work using the CFEM has been done to investigate important issues in fracture mechanics such as terminal crack speed and crack branching [10], interfacial fracture [11], and material fragmentation [12]. These investigations have led to a better understanding of the fracture processes at the microscopic level.

The CFEM is particularly advantageous in characterizing arbitrary nature of the dynamic fracture processes [8–10,13–16]. In a regular finite element scheme, bulk elements are perfectly bonded. Therefore, separation is possible only if additional criteria are used and the finite element connectivity is revised during calculations, as in the element deletion method. On the other hand, in the CFEM, the element boundaries are kinematically separate. To simulate complex crack patterns associated with crack deflection, branching, and microcracking, cohesive elements can be specified along all finite element boundaries to serve as potential crack paths [10,14,15]. The CFEM provides a useful tool for exploring the quantitative features of the fracture processes through explicit simulations. Since the failure has been incorporated into a cohesive law, the CFEM does not require any crack initiation and propagation criterion in the numerical implementation. The cohesive formulation allows fracture to evolve as a natural outcome of the combined effects of bulk constituent response, interfacial behavior, and applied loading. However, none of the aforementioned work considered microstructures of heterogeneous materials.

There have been efforts to incorporate microstructures into the simulations by CFEM. Espinosa and Zavattieri [17,18] employed the CFEM to analyze the response of alumina microstructures under quasi-static and dynamic loading and assessed the roles of grain boundary strength and toughness, their stochasticity, and separation rate on damage initiation and evolution. Zavattieri and Espinosa [19] presented a grain-level micromechanical analysis of alumina microstructures subject to dynamic compression-shear loading. In these simulations, the cohesive elements were inserted only along grain boundaries to phenomelogically capture intergranular fracture through breaking of atomic bonds or grain boundary sliding. One obvious shortcoming is that transgranular fracture in the microstructures cannot be captured.

Zhai and Zhou [20] and Zhai et al. [21] used the exponential cohesive law [10] and a bilinear cohesive law in the CFEM to explicitly account for arbitrary microstructures and fracture patterns in Al_2O_3/TiB_2 ceramic composites. They demonstrated the effects of microstructures, material inhomogeneities, and interfacial strength on dynamic fracture characteristics. In these simulations, to simulate complex crack patterns associated with crack deflection, branching, and microcracking, the cohesive elements were specified along all bulk finite element boundaries to serve as potential crack paths. Tomar et al. [22] studied lower and upper bounds for CFEM models with intrinsically embedded cohesive surfaces and cohesive laws with finite initial stiffness. They found that the element size must be small enough to accurately resolve the stress distribution inside the cohesive zones at crack tips. On the other hand, the cohesive surface contribution to stiffness reduction must be small, such that wave speed in the solid is not affected due to the presence of cohesive surfaces. This imposes a lower bound on the size of the elements.

In this paper, we develop a micromechanical approach for determining the fracture toughness of the AZ31 Mg alloy at the microscopic level. To assist the study on the effect of the microstructures on the fracture toughness, we employ a multi-order parameter phase-field model with an active parameter tracking (APT) algorithm to generate microstructures with systematically varying attributes. To capture both intergranular and transgranular fracture, we follow the approach of Zhai and Zhou [20] and Zhai et al. [21] by specifying the cohesive elements along all bulk finite element boundaries and using very fine meshes to resolve arbitrary crack paths and microcrack patterns. The design of mesh and specification of cohesive law parameters follow the convergence criterion of Tomar et al. [22]. The analysis will focus on the FPZ evolution and its interaction with different microstructure heterogeneities. The effects of microstructural variance and overall strain rate on the fracture toughness of the AZ31 Mg alloy will be characterized.

2. Simulation methodology – cohesive finite element method

The CFEM is well suited for the simulation of the separation processes in fracture. Spatially-distributed cohesive elements within the FPZ concern all material entities. Specifically, the CFEM model consists of conventional bulk elements and cohesive elements along all bulk element boundaries. Constitutive relations must be specified for all the bulk elements, as in the regular FEM. In addition, cohesive laws which relate tractions and interfacial separations are needed to fully characterize the behavior of cohesive elements.

Here, an elasto-plastic, isotropic constitutive relation is assumed for the bulk constituents, namely, the grain interiors (GIs), the grain boundary-affected zones (GBAZs), and homogenized alloy (HA) zones (details in Section 3). An additive decomposition of the rate of deformation is employed, i.e.,

$$\mathbf{D} = \mathbf{D}^e + \mathbf{D}^p, \tag{1}$$

where $\mathbf{D}$ is the total rate of deformation, $\mathbf{D}^e$ is the elastic part of the rate of deformation, and $\mathbf{D}^p$ is the plastic part of the rate of deformation [23]. Small elastic strains and elastic isotropy are presumed so that

$$\mathbf{D}^e = \mathbf{L}^{-1} : \hat{\tau}, \tag{2}$$

where $\mathbf{L}$ is the tensor of isotropic elastic moduli and $\hat{\tau}$ is the Jaumann rate of Kirchhoff stress. Plastic flow follows the J_2-plasticity rule, i.e.,

$$\mathbf{D}^p = \frac{3\dot{\bar{\varepsilon}}_p}{2\bar{\sigma}}\tau', \tag{3}$$

where $\bar{\sigma}$ is the von Mises stress, τ' is the devitoric stress, and $\dot{\bar{\varepsilon}}_p$ is the effective plastic strain rate defined as

$$\dot{\bar{\varepsilon}}_p = \sqrt{\frac{2}{3}\mathbf{D}^p : \mathbf{D}^p}. \tag{4}$$

The Johnson–Cook model [24] is employed to describe the constitutive behavior of the bulk elements, i.e.,

$$\sigma(\dot{\varepsilon}) = \sigma(\dot{\varepsilon}_0)\left(1 + C\ln\frac{\dot{\varepsilon}}{\dot{\varepsilon}_0}\right), \tag{5}$$

where $\dot{\varepsilon}_0$, a reference strain rate, is taken as 10^{-3} s^{-1}; $\sigma(\dot{\varepsilon}_0)$, a reference stress–strain curve at the reference strain rate, can be found in Lou et al. [25]; and C, a strain-rate sensitivity constant, is taken as 0.02. All material constitutive parameters in $\sigma(\dot{\varepsilon}_0)$ are chosen at the room temperature.

The cohesive law specifies the relationship between traction and separation across the cohesive surfaces. Many cohesive laws have been proposed for different conditions. Here, the bilinear cohesive law for mixed-mode fracture is employed [21]. The fracture energy G_F is the work required to create and fully separate a unit surface area pair and is given by

$$G_F = \int_0^{w_c} T(w)dw, \tag{6}$$

where T is the effective traction, w is the effective separation, and w_c is the critical separation beyond which the traction becomes zero and the cohesive element is regarded as having failed completely. The effective traction T and the effective separation w are defined as

$$T = \sqrt{T_n^2 + T_t^2} \quad \text{and} \quad w = \sqrt{w_n^2 + w_t^2}, \tag{7}$$

respectively. In the above relations, T_n and T_t are the cohesive tractions in the normal and tangential directions, respectively; and w_n and w_t are the normal and tangential separation across the cohesive surfaces, respectively. The normal and tangential tractions T_n and T_t across the cohesive surfaces are given by, respectively,

$$T_n = T\frac{w_n}{w} \quad \text{and} \quad T_t = T\frac{w_t}{w}. \tag{8}$$

For the bilinear cohesive law,

$$T = \begin{cases} T_m \frac{w}{w_m} & \text{for } 0 \leqslant w \leqslant w_m; \text{ and} \\ T_m \frac{w_c - w}{w_c - w_m} & \text{for } w_m < w \leqslant w_c. \end{cases} \tag{9}$$

In the above relations, T_m is the cohesive traction at which damage initiates and w_m is the characteristic separation at which the effective cohesive traction T reaches the cohesive strength T_m.

Fig. 1 gives a schematic illustration of the relation between T and w. Apparently, three cohesive parameters, e.g., the cohesive strength T_m, the characteristic separation w_m, and the critical separation w_c, are needed to characterize the bilinear cohesive relation. The deformation of a cohesive element consists of two stages. In the initial stage (O-A), the separation is elastic and the cohesive energy stored during this stage is recoverable. In the second stage (A-B), the separation leads to material degradation and linear softening associated with the initiation and evolution of damage. The cohesive energy consumed for the crack surface formation during the second stage is partially irrecoverable. The characteristic separation w_m reflects the proportion of the first stage in the whole process. From Fig. 1, it can be found that w_m influences the slope of O-A, i.e., the

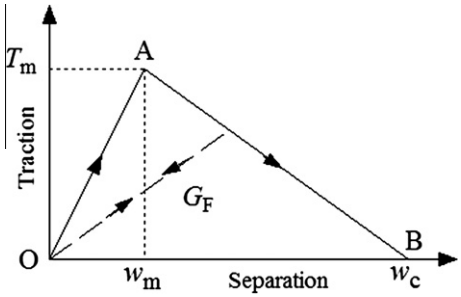

Fig. 1. Bilinear cohesive law.

stiffness of the cohesive element. Lower w_m values (under contact values of T_m) indicate stiffer cohesive response. A damage parameter for cohesive separation, D, can be defined as [26]

$$D = \frac{w_c(w - w_m)}{w(w_c - w_m)}. \tag{10}$$

Obviously, $D = 0$ initially. After total failure occurs, $D = 1$. D can be employed as a measure for damage in crack surfaces. The CFEM model is implemented in ABAQUS [26].

3. Determination of fracture toughness

3.1. Phase-field model for grain growth

Controlling microstructure evolution is crucial to optimization of materials properties through processing. Therefore, there have been much computational efforts in materials science to model microstructural transformations under realistic conditions. Multiple approaches for simulating grain growth have been developed, including Monte Carlo models [27], vertex tracking [28], front tracking [29], Laguerre tessellation [30], cellular automata [31], and phase-field approaches [32–36]. For coarsening of a polycrystalline solid with uniform grain-boundary mobilities and energies, all of these approaches reach similar conclusions on the kinetic and topological aspects of two-dimensional grain growth [37]. The main advantage of the phase-field grain growth approach over the vertex tracking, the front tracking, Laguerre tessellation, and the cellular automata methods is that it has no need to track the positions of interfaces. The advantage of the phase-field grain growth approach over the Monte Carlo approach is the accuracy of the grain boundary curvature representation. Therefore, the phase-field grain growth approach is an appealing approach for generating microstructures with systematically varying attributes.

Chen and Yang [32] proposed a multi-order parameter phase-field grain growth model. In the model, a grain structure is described by a set of order parameters $(\eta_1, \eta_2, \ldots, \eta_Q)$, with each order parameter corresponding to a different grain orientation. The following time-dependent equations for each order parameter can be solved [32,37]

$$\frac{\partial \eta_i}{\partial t} = -M_i\left(\frac{\delta F}{\delta \eta_i}\right), \quad i = 1, 2, \ldots, Q, \tag{11}$$

where M_i denote grain boundary mobilities and F is the total free energy of the system. In the simulations reported here, M_i have identical and constant values. The free energy is a function of the order parameters and their gradients [32,37], i.e.,

$$F = \int_V \left[f_0(\eta_1, \eta_2, \ldots, \eta_Q) + \frac{1}{2}\sum_{i=1}^{Q} \kappa_i (\nabla \eta_i)^2 \right] dV, \tag{12}$$

where f_0 represents local free energy density, and κ_i are the gradient energy coefficients. For a system containing a finite number of grains, with each grain having one of Q possible orientations, function f_0 can be chosen to have degenerate minima at $(\eta_1, \eta_2, \ldots, \eta_Q) = (1,0,\ldots,0), (0,1,\ldots,0), \ldots, (0,0,\ldots,1)$. A simple function f_0 satisfying this requirement is given as [32,37]

$$f_0(\eta_1, \eta_2, \ldots, \eta_Q) = \sum_{i=1}^{Q}\left(-\frac{1}{2}\alpha \eta_i^2 + \frac{1}{4}\beta \eta_i^4\right) + \gamma \sum_{i=1}^{Q}\sum_{j \neq i}^{Q} \eta_i^2 \eta_j^2, \tag{13}$$

where α, β, and γ are phenomenological constants. For $\alpha = \beta > 0$ and $\gamma > \beta/2$, f_0 has $2Q$ minima at $\eta_j = \pm 1$ and $\eta_i = 0$ for all $i \neq j$. Substitution of Eqs. (12) and (13) into Eq. (11) yields the equation of motion [32,37]

$$\frac{\partial \eta_i}{\partial t} = -M_i\left(-\alpha \eta_i + \beta \eta_i^3 + 2\gamma \eta_i \sum_{j \neq i}^{Q} \eta_j^2 - \kappa_i \nabla^2 \eta_i\right). \tag{14}$$

Owing to the implementation of the APT algorithm to improve computational efficiency and to avoid early-stage unphysical grain coalescence [38], Eq. (14) has to be solved only at and near the grain boundaries using a forward-Euler integration scheme [32,37]

$$\eta_i(t + \Delta t) = \eta_i(t) + \frac{d\eta_i}{dt}\Delta t \tag{15}$$

Since the APT algorithm is implemented in the model of Chen and Yang [32], an order parameter is associated with a unique grain orientation in the grain structure. This algorithm avoids unphysical grain coalescences seen in previous studies [32,37], where one order parameter is associated with multiple grains. Another advantage of the APT algorithm [38] is computation efficiency. The number of active order parameters in a two-dimensional grain growth simulation is typically 20–30. Therefore, only 1–30 Ginzburg–Landau equations at each point instead of Q (2000 in the calculations carried out here) equations need to be solved.

The two-dimensional calculations carried out involve 500×500 grid points and a grid spacing of $\Delta x = 2.0$ with periodic boundary conditions in all directions. The initial structure has 2000 circular grains of radius $2.0\ \Delta x$. No overlap between the initial grains is permitted. The coefficients in Eq. (13) are $\alpha_i = \beta_i = \gamma_i = 1$, $\kappa_i = 2$, and $M_i = 1$ for all i. The grain boundary energy

and mobility are isotropic. The time step size Δt in Eq. (15) is taken as 0.1. Grain structures for six different time steps and with a size of 0.17 × 0.17 mm are shown in Fig. 2a–f and their central regions with the dimensions of 0.08 × 0.08 mm are shown in Fig. 2h–l. The total number of grains decreases from 1160 to 113 as the average grain size increases from 9.4 to 32.2 μm. Green zones represent GIs, blue zones represent GBAZs, and red lines represent interfaces between the GIs and the GBAZs.

3.2. Computational framework for determination of fracture toughness

One issue in evaluating fracture toughness in heterogeneous materials resides in the fact that both large and small scale features must be considered concurrently. The reason is that fracture toughness is a macroscopic quantity while fracture mechanisms typically are operative at the microscale [39]. To satisfy the requirements for fracture toughness testing set forth in ASTM standard E399 [40], a center-cracked-tension (CCT) specimen with a width of 320 mm, a height of 160 mm, and a central pre-crack length of 160 mm, is employed in this study. The configuration used in the analysis is shown in Fig. 3. The microstructure region with a size of 0.17 × 0.17 mm is placed in front of the pre-crack tip. A close-up view of its central region with a size of 0.08 × 0.08 mm is also shown in Fig. 3. Unless otherwise stated, the pre-crack tip extends 20 μm into the microstructure. The fine meshes consisting of cross-triangular elements (1 μm in size) are used to resolve the microstructure morphology of the material and fracture development. Note that the bulk elements in the microstructure have exactly the same size in this study so that the embedded cohesive elements have exactly the same number density for the different microstructures to exclude the dependence of simulation results on the number density of the cohesive elements [41]. Outside the microstructure region, the material is taken as an isotropic HA with the macroscopic properties of the material analyzed. The number of bulk elements (3-node triangular continuum plain strain element, i.e., CPE3 in ABAQUS)

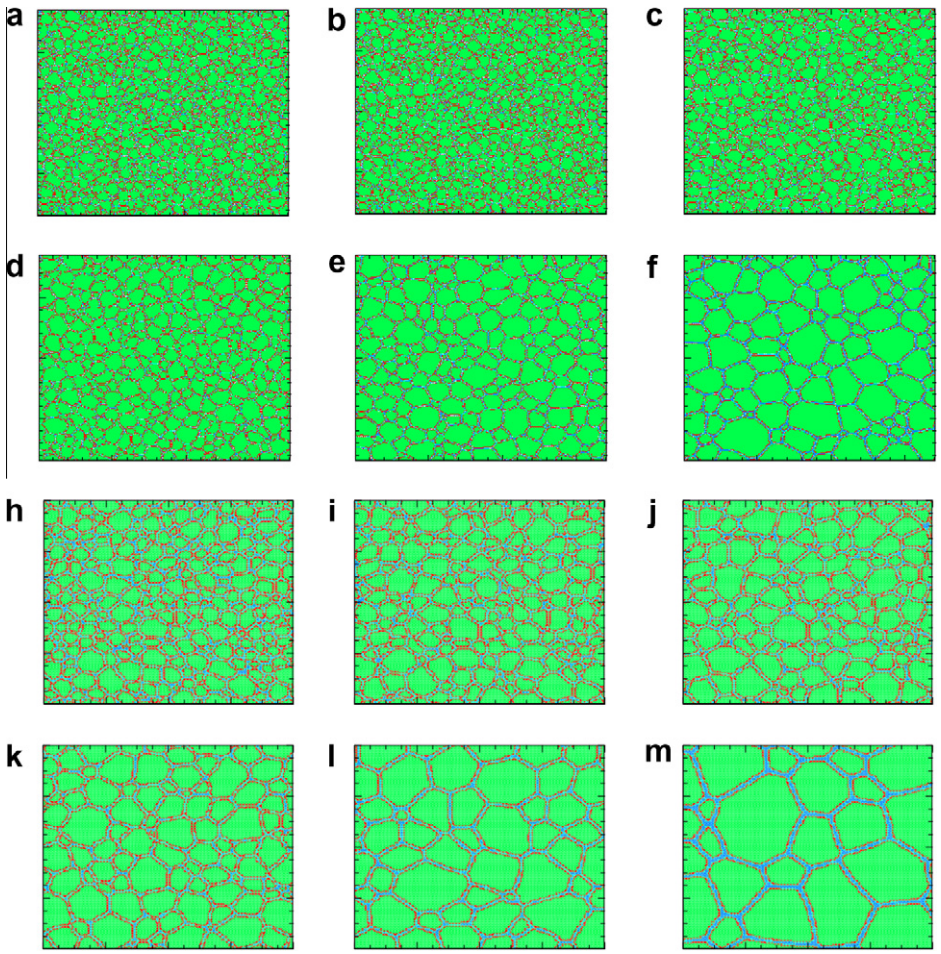

Fig. 2. Microstructures with each size 0.17 × 0.17 mm and their close-up views with each size 0.08 × 0.08 mm generated by phase-field grain growth simulations: (a) average grain size: 9.37 μm, (b) average grain size: 11.32 μm, (c) average grain size: 12.86 μm, (d) average grain size: 16.38 μm, (e) average grain size: 22.85 μm, (f) average grain size: 32.17 μm, (g) close-up view of (a), (h) close-up view of (b), (i) close-up view of (c), (j) close-up view of (d), (k) close-up view of (e), (l) close-up view of (f).

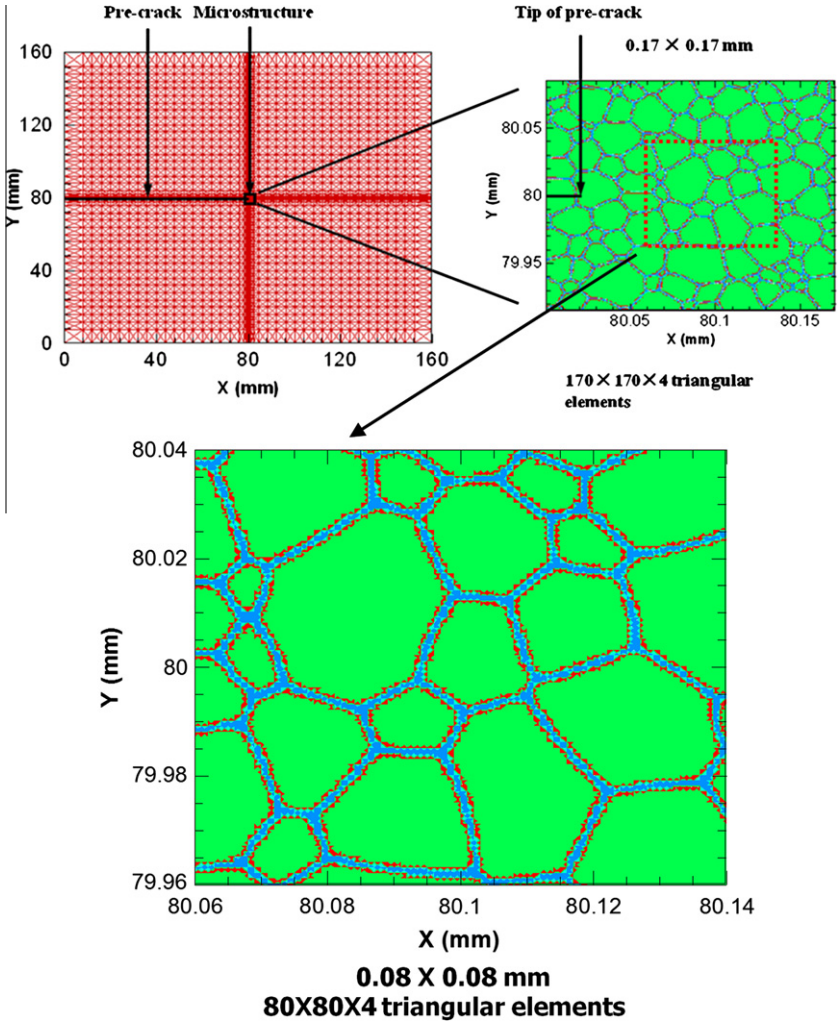

Fig. 3. Configuration of fracture analyses.

is over 305,000 and the number of cohesive elements (2-dimensional 4-node cohesive elements, i.e., COH2D4 in ABAQUS) is over 456,000. As required by ASTM E399 [40], plain strain condition is used in the simulations.

In Espinosa and Zavattieri [17,18], the grain boundaries are discrete lines with zero thickness and cohesive elements are inserted only along the grain boundaries. Their results demonstrated that stress concentration is only present in the case with grain anisotropy and that the presence of the cohesive elements does not affect the uniform stress distribution observed in the isotropic case. In this paper, each phase (GI, GBAZ, and HA in Fig. 3) is taken to be isotropic and non-uniform stress distributions can occur due to the introduction of the GBAZs with non-zero thickness and, therefore, finite volume.

Although the GIs and the GBAZs are intrinsically anisotropic due to the crystalline structure and triple junctions, in the "composite" model for the crystalline grain structure, to treat each phase as an isotropic constituent has proven to be a rational approximation to describe the overall mechanical behaviors of the grain structure [42]. Furthermore, while some theoretical models can be anisotropic, in order to simplify the subsequent computation, the phases can be considered isotropic to capture the main mechanical issues [43,44].

The grain interior (GI) has a higher yield stress and lower fracture energy than the GBAZ. Table 1 lists the properties of the HA, GI and GBAZ. Specifically, compared with the HA, the GI's yield stress is 10% higher and its cohesive strength is 10% lower, while the GBAZ's yield stress is 20% lower and its cohesive strength is 20% higher. The cohesive strength of the interface between the GI and the GBAZ is 10% higher than that of the HA. The critical separations for the GI, the GBAZ, the interface, and the HA are taken to be the same and equal to w_c, as listed in Table 1.

Among the cohesive strength, the critical separation, and the fracture energy, only two out of the three are independent. In this paper, the fracture energy G_F is taken as, unless otherwise stated, 7500 J m^{-2} (corresponding to a fracture toughness of 19.6 MPa$\sqrt{\text{m}}$). As illustrated in Fig. 4, in the bilinear cohesive law, as the cohesive strength T_m increases from 500 to 600 MPa, the critical separation w_c correspondingly decreases from 30 to 25 μm, which is over 25 times the element size in the

Table 1
Constitutive parameters for bulk materials and cohesive surfaces.

Compound	Density ($kg\,m^{-3}$)	Yield stress	Elastic modulus (GPa)	Poisson's ratio	Cohesive strength (GPa)	Critical separation (μm)	Fracture energy ($J\,m^{-2}$)
Grain boundary-affected zone (GBAZ)	1738	$0.8\sigma_0$	45	0.35	$1.2T_m$	w_c	$1.2G_F$ (600 $T_m w_c$)
Grain interior (GI)	1738	$1.1\sigma_0$	45	0.35	$0.9T_m$	w_c	$0.9G_F$ ($450T_m w_c$)
Interface	...	...	...	...	$1.1T_m$	w_c	$1.1G_F$ ($550T_m w_c$)
Homogenized alloy (HA)	I738	σ_0	45	0.35	T_m	w_c	G_F ($500T_m w_c$)

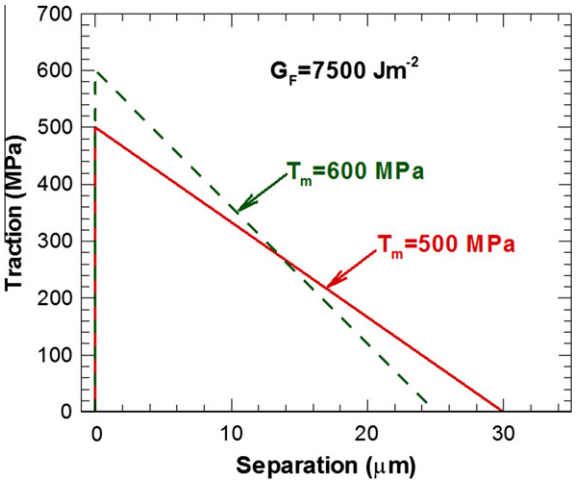

Fig. 4. Bilinear cohesive relations used in the simulations.

microstructure region. This leads to large distortion and crack blunting around the crack tip. In all simulations, the characteristic separation w_m is taken as 0.01 μm, which is much smaller than the critical separation w_c, to restrict artificial softening of global stiffness and mesh dependence due to the insertion of the cohesive elements [22]. As a result, traction increases rapidly before T_m is reached and then decreases slowly, as shown in Fig. 4.

Symmetric velocity boundary conditions are imposed at the bottom and top edges of the specimen in Fig. 3. During the simulation, the reaction force at each boundary node at the bottom or top edges is used to obtain P, the load at the upper or lower boundary of the CCT specimen. For the CCT specimen configuration considered, the stress intensity factor can be calculated as [40,45]

$$K = \frac{P}{B\sqrt{W}}\sqrt{\frac{\pi a}{4W}\sec\left(\frac{\pi a}{2W}\right)}\left[1 - 0.025\left(\frac{a}{W}\right)^2 + 0.06\left(\frac{a}{W}\right)^4\right], \tag{16}$$

where W, half width of the CCT specimen, is 160 mm; a, half length of the central-crack, is 80 mm; B, specimen thickness, is 1.0 m since plain strain conditions are required to prevail.

4. Trends in fracture toughness of the AZ31 Mg alloy

4.1. CFEM results and comparison with K-field theory

The CFEM does not require any crack initiation or propagation criterion in the numerical implementation. For the purpose of consistent identification of crack initiation, an empirical criterion is specified to define the critical point of fracture initiation and the corresponding stress intensity factor which is taken as the fracture toughness of the material.

Unless otherwise stated, the overall strain rate is 0.0125 s^{-1} so that the specimen is in a quasi-static loading state. In the first example, for the HA, the cohesive strength T_m is 570 MPa (~3.0 times its yield stress σ_0 (187.5 MPa)). The constitutive parameters for the other phases can be obtained from the relationships in Table 1. Since the overall fracture toughness is 19.6 $MPa\sqrt{m}$, the relation between the stress intensity factor and the opening displacement δ of the pre-crack tip can be used to determine the critical crack tip opening displacement (CTOD) δ_{cr} as

$$\delta_{cr} = \delta_{cr0} = 10\ \mu m. \tag{17}$$

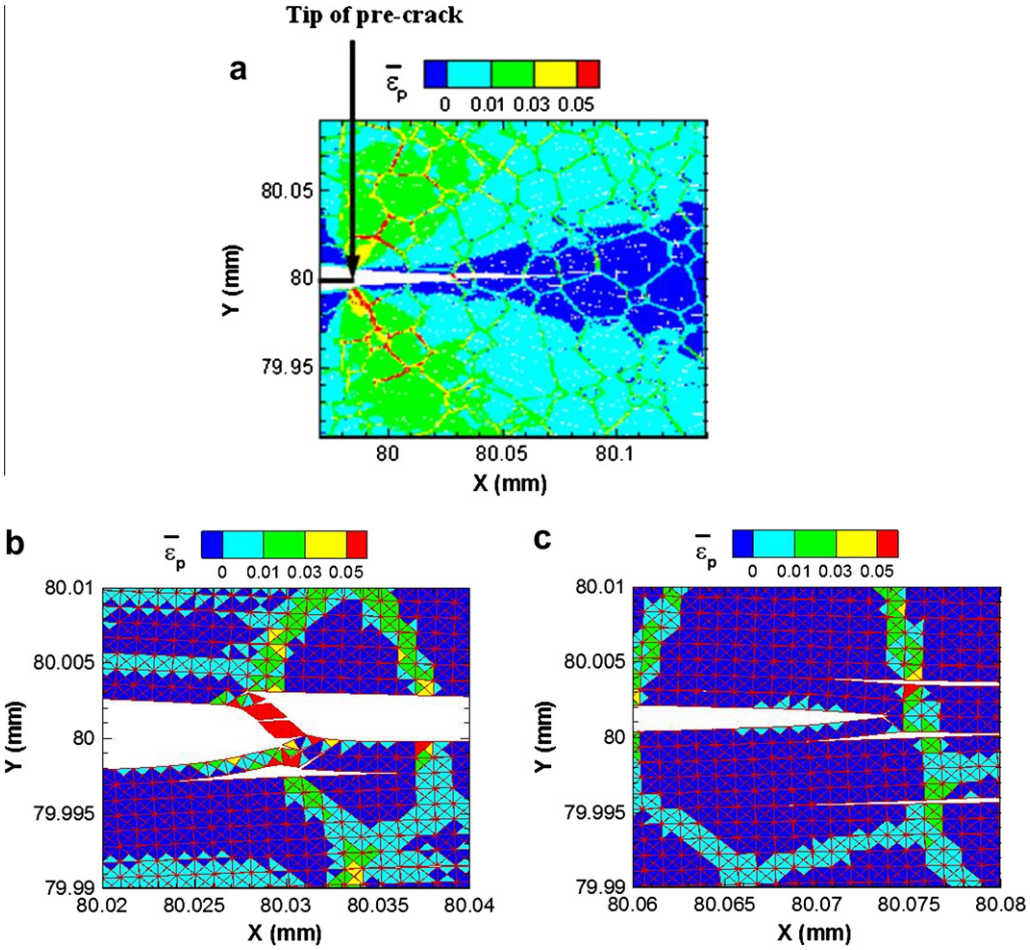

Fig. 5. Equivalent plastic strain in the microstructure at fracture initiation in deformed configuration: (a) obtained from CFEM simulation, (b) the first close-up view of (a) (with mesh), (c) the second close-up view of (a) (with mesh).

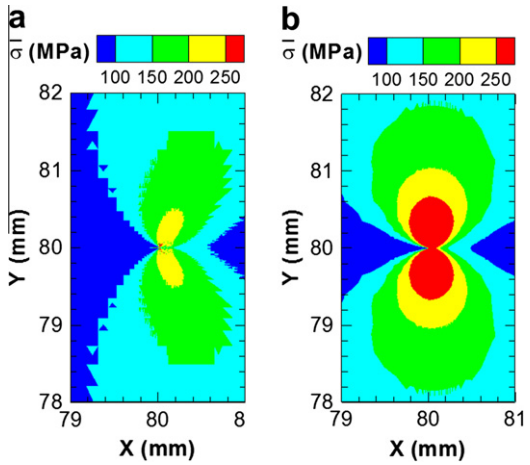

Fig. 6. Distribution of $\bar{\sigma}$ around the pre-crack tip: (a) obtained from CFEM simulation and (b) obtained from K-field theory at $K = 18.4\ \mathrm{MPa}\sqrt{\mathrm{m}}$.

This condition is used to define crack initiation and identify the fracture toughness. Eq. (17) is used in the calculations and updated accordingly, as shown in subsequent context.

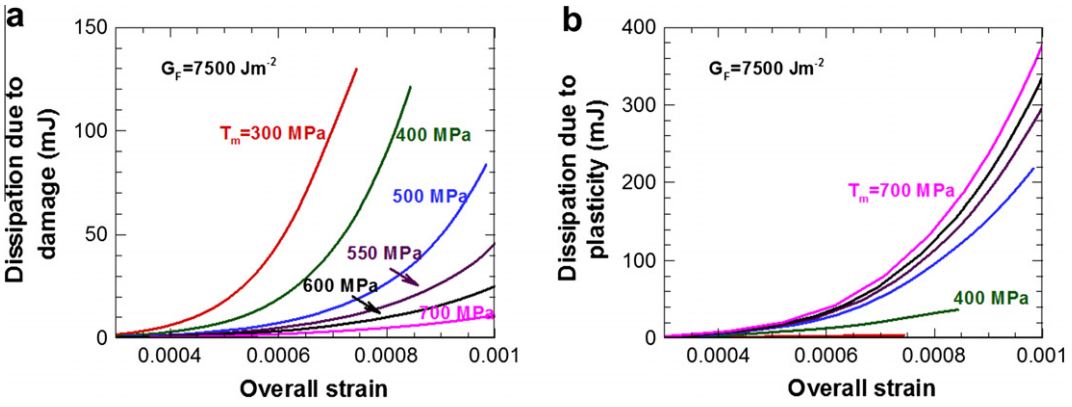

Fig. 7. Dissipation due to damage and plasticity as functions of overall strain at different levels of cohesive strength: (a) dissipation due to damage and (b) dissipation due to plasticity.

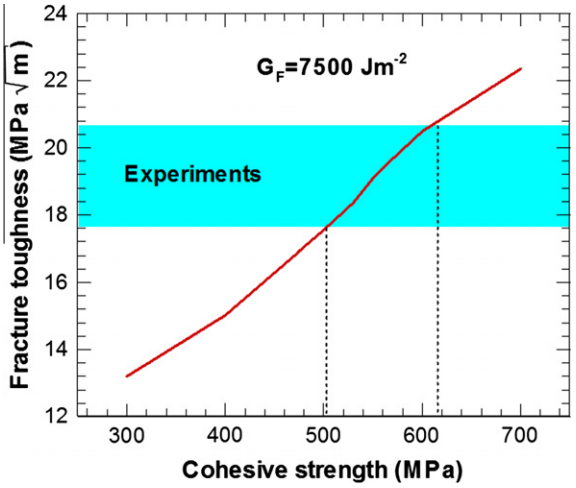

Fig. 8. Effect of cohesive strength on the fracture toughness of the Mg alloy.

The crack opening displacement of δ_{cr} = 10 μm is used for other microstructures as well. For the HA, the cohesive strength T_m is taken as 550 MPa ($\sim 2.9\sigma_0$). The fracture toughness is determined to be 18.4 MPa$\sqrt{m}$. Fig. 5a shows the distribution of the equivalent plastic strain $\bar{\varepsilon}_p$ in the microstructure region when fracture initiation occurs (condition in Eq. (17) is met). It can be seen that the equivalent plastic strain in the GBAZs is clearly higher than that in the nearby GIs. This observation is consistent with the understanding of failure of metals. Fig. 5b and c with the bulk and cohesive elements are close-up views of Fig. 5a. Both of them clearly show the smaller $\bar{\varepsilon}_p$ along the main crack due to unloading. Fig. 5b illustrates the heavily-deformed debris bridging two faces of the main crack and a microcrack nucleated nearby, while Fig. 5c illustrates the nucleation of three microcracks in front of the main crack tip. All of the four nucleated microcracks in Fig. 5b and c intersect the GBs. Fig. 6a shows the distribution of the von Mises stress $\bar{\sigma}$ in the pre-crack tip region when fracture initiation occurs. For comparison, Fig. 6b shows the K-field stress distribution at $K = 18.4$ MPa$\sqrt{m}$. The von Mises yield criterion is employed to estimate the elastic–plastic boundary and thus the plastic zone size. The plastic zone size (yellow[1] region in Fig. 6a) obtained by CFEM calculations (plane strain condition) is ~50% that predicted by the *K*-field theory (plane strain condition). Our results are in good agreement with finite element analysis [46]. The agreement is better in the *Y* direction.

4.2. Dependence of fracture toughness on cohesive strength

The fracture behavior predicted by the CFEM model depends heavily on the cohesive strength T_m and the fracture energy G_F specified through the cohesive law. The effects are analyzed in detail here. Effect of the cohesive strength on the overall fracture toughness is studied first. Six levels of cohesive strength T_m, i.e., 300 ($\sim 1.6\sigma_0$), 400, 500, 550, 600, and 700 MPa

[1] For interpretation of color in Figs. 2 and 6, the reader is referred to the web version of this article.

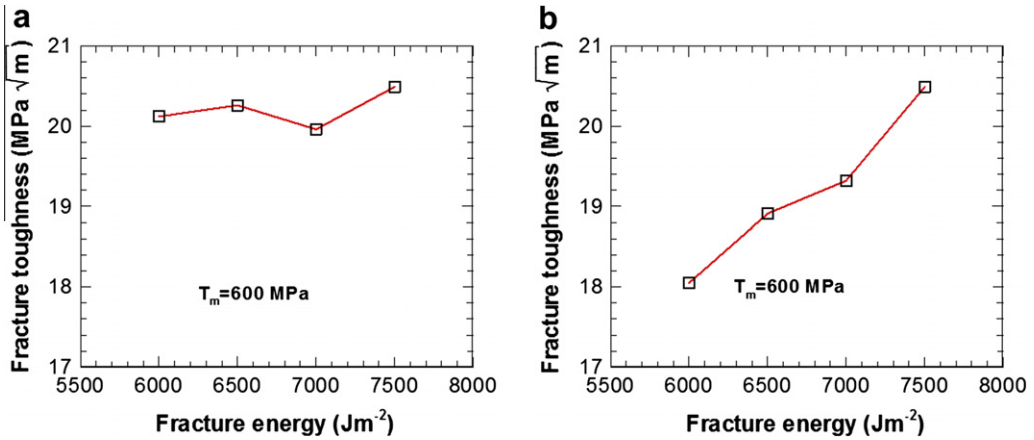

Fig. 9. Effect of HA fracture energy on overall fracture toughness at two levels of crack-tip opening displacement: (a) when Eq. (17) is used and (b) when Eq. (18) is used.

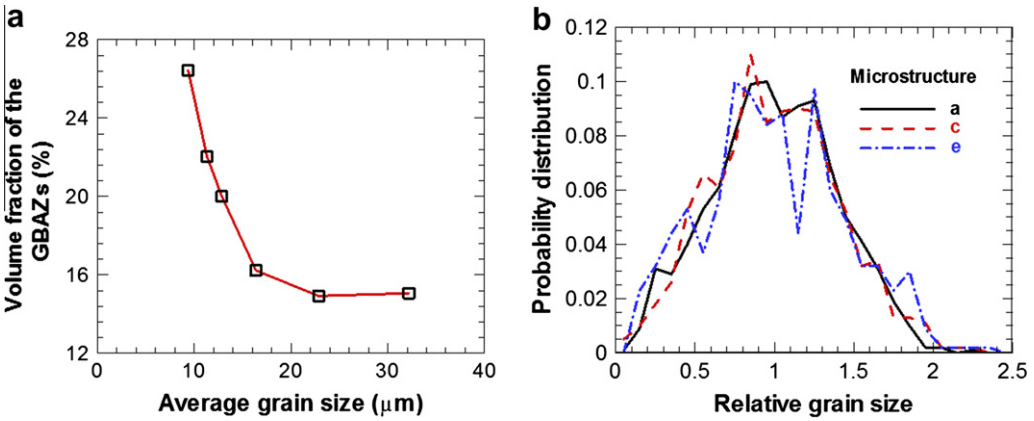

Fig. 10. Volume fraction of the GBAZs and distribution of relative grain size for three of the microstructures in Fig. 2: (a) volume fraction of the GBAZs and (b) probability distribution of relative grain size.

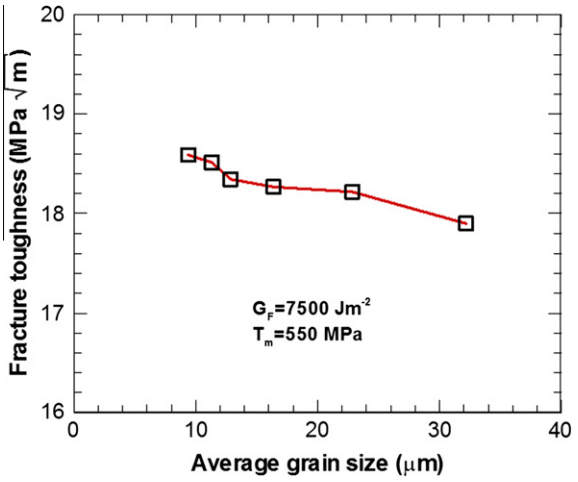

Fig. 11. Effect of the average grain size on the fracture toughness of the Mg alloy.

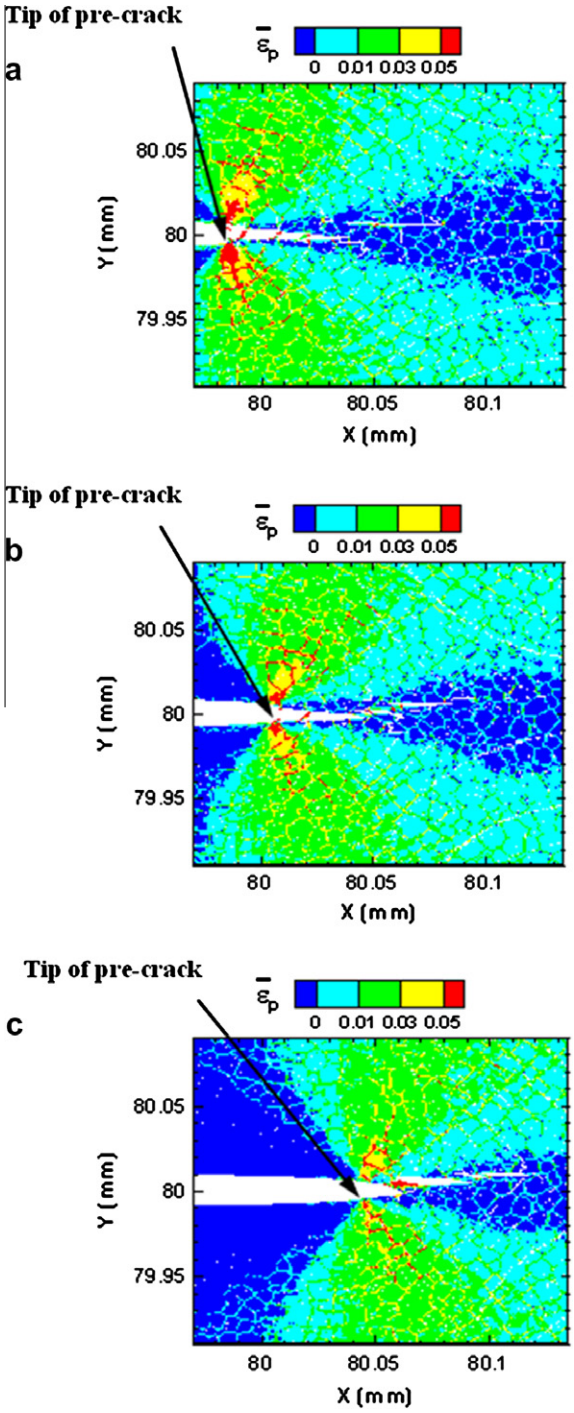

Fig. 12. Effect of the local environment around the pre-crack tip on the fracture toughness (in deformed configuration): (a) the pre-crack tip extends 20 μm into the microstructure, (b) the pre-crack tip extends 40 μm into the microstructure, (c) the pre-crack tip extends 80 μm into the microstructure.

($\sim 3.7\sigma_0$), are considered. The results show that the total external work and strain energy do not change with the cohesive strength essentially. This can be explained by the fact that both of these quantities are associated with the bulk deformation process, i.e., they are mostly related to bulk elasticity and plasticity and are insensitive to the fracture process. On the other hand, the dissipations due to damage and plasticity are quite sensitive to the cohesive strength, as shown in Fig. 7. The fracture toughness values of the AZ31 Mg alloy with the different cohesive strength levels are shown in Fig. 8. Experiments show that the fracture toughness of the AZ31 Mg alloy varies from 17.6 to 20.7 MPa$\sqrt{\text{m}}$ [3,4], as illustrated as the colored band in

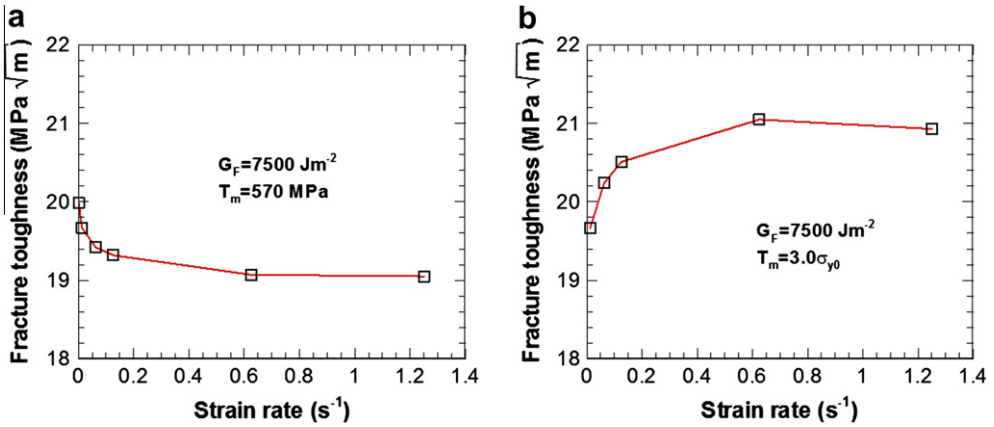

Fig. 13. Effect of cohesive law on fracture toughness: (a) rate-independent cohesive strength and (b) rate-dependent cohesive strength.

Fig. 8. Obviously, cohesive strength values between 505 MPa and 615 MPa provide the best fit to the experimental results. These values are 2.7–3.3σ_0 of the AZ31 alloy as reported in the literature.

4.3. Dependence of fracture toughness on fracture energy

Next, effect of the fracture energy of the HA on the overall fracture toughness is studied. The cohesive strength T_m is taken to be 600 MPa and four levels of the HA fracture energy G_F (6000, 6500, 7000, and 7500 J m^{-2}) are considered. In Fig. 9a, the critical CTOD values in Eq. (17) are used. In Fig. 9b, the critical CTOD is taken to be proportional to the fracture energy of the HA, i.e.,

$$\delta_{\mathrm{cr}} = \frac{G_F}{G_{F0}}\delta_{\mathrm{cr0}} = \frac{G_F}{7500\ \mathrm{J\ m^{-2}}}10\ \mu\mathrm{m}. \tag{18}$$

When Eq. (18) is used, the fracture toughness increases with the fracture energy (as shown in Fig. 9b). This result is consistent with the generally accepted trends. It has been shown that the critical CTOD is proportional to the fracture energy (see, e.g., [45]).

4.4. Dependence of fracture toughness on grain size

The dependence of fracture toughness on grain size is an important issue for metallic alloys as it provides a mechanism for toughening through microstructure modification. The microstructures in Fig. 2 are used in the analysis in this regard. Fig. 10a illustrates that the volume fraction of the GBAZ decreases from 26% to 15% as the average grain size increases from 9.4 to 32.2 μm in Fig. 2. To quantify the variations in grain size, we define the relative size of each grain as the ratio of its size to the average grain size in the microstructure. Fig. 10b illustrates the distributions of the relative grain size for three of the microstructures in Fig. 2. The distributions are essentially the same, indicating that the only difference between the microstructures is the average grain size and the relative size distributions are consistent with each other.

In the simulations, the cohesive strength T_m for the HA is taken as 550 MPa (~2.9σ_0). Since the primary interest here is on the effect of the geometric aspect of the microstructures, both the bulk and cohesive properties of the phases are kept constant. Fig. 11 shows that the overall fracture toughness decreases from 18.6 to 17.9 MPa$\sqrt{\mathrm{m}}$ as the average grain size increase from 9.4 to 32.2 μm. Somekawa and Mukai [5] improved fracture toughness of the AZ31 Mg alloy by refining the grain structure through an ECAE process. The simulation results here agree reasonably well with the trend in the experiments of Somekawa and Mukai [5].

4.5. Dependence of fracture toughness on local environment at the pre-crack tip

Effect of the local environment at the pre-crack tip on the overall fracture toughness is also investigated. A microstructure with an average grain size of 14.9 μm is chosen and the associated fraction of the GBAZ is 17.6%. The cohesive strength T_m is taken to be 550 MPa. The pre-crack tip extends 20, 40, and 80 μm into the same microstructure in Fig. 12a–c to provide a random sampling of the crack tip location. Note that the differences in the crack lengths here are less than 1/1000 of the overall crack length (Fig. 3), therefore, have negligible effect on the evaluation of fracture toughness in the analysis. Upon fracture initiation, the distribution of the equivalent plastic strain and the fracture patterns are dramatically different between the cases studied. Furthermore, the overall fracture toughness is 19.38 MPa$\sqrt{\mathrm{m}}$ for the 20 μm-extension, 18.85 MPa$\sqrt{\mathrm{m}}$ for the 40 μm-extension, and 19.17 MPa$\sqrt{\mathrm{m}}$ for the 80 μm-extension. This effect is clearly appreciable. The

relative variation in the fracture toughness is approximately 2.8%, giving an estimate for the degree of variation in K_{IC} estimate for each microstructural setting.

4.6. Dependence of fracture toughness on overall strain rate

Finally, the effect of the overall strain rate on the fracture toughness is studied. The dependence of the stress–strain relation on strain rate is characterized by the Johnson–Cook model (Eq. (5)). A constant cohesive strength T_m = 570 MPa ($\sim 3.0\sigma_0$) is used. The fracture toughness decreases as the overall strain rate increases, as shown in Fig. 13a. To further analyze the issue, a rate-dependent cohesive law is used. Specifically, the cohesive strength is take to be

$$T_m = T_m(\dot{\varepsilon}) = 3.0\sigma_0(\dot{\varepsilon}) = 3.0\sigma_0(\dot{\varepsilon}_0)\left(1 + 0.02\ln\frac{\dot{\varepsilon}}{\dot{\varepsilon}_0}\right). \tag{19}$$

The results are shown in Fig. 13b. Under this condition, the fracture toughness is found to increase with strain rate. The qualitatively different trends in Fig. 13 are in contrast to each other. Validation by experiments or molecular dynamic simulations should provide more insight in this regard.

5. Conclusions

A micromechanical approach based on the CFEM for quantifying the fracture toughness of the AZ31 Mg alloy as functions of microstructure is developed. To study the effect of microstructure on the fracture toughness of this material, a multi-order parameter phase-field grain growth model with the APT algorithm is employed to generate microstructures with systematically varying attributes. In the analysis, each phase (the GI, the GBAZ, and the HA) is taken as an isotropic constituent. The evolution of the FPZ and its interaction with the microstructure are investigated. The cohesive strength for the AZ31 Mg alloy is calibrated by comparing the fracture toughness results from CFEM simulations with those from experimental studies reported in the literature. Two different trends of the overall fracture toughness as a function of the fracture energy of the HA have been identified, depending on the nature of the critical CTOD. Simulations show that the overall fracture toughness increases as the average grain size decreases. The fracture toughness also depends on the nature of the cohesive law used. While strain rate hardening of the bulk constituents causes the fracture toughness to be lower at higher strain rates, strain rate hardening of the cohesive surfaces cause the fracture toughness to increase as strain rate increases. The findings that both the nature of the critical CTOD (its dependence on the fracture energy) and that of the cohesive law (its dependence on strain rate) dramatically alter and even directly reverse the trend of the fracture toughness suggest a need to carefully choose the critical CTOD and the cohesive law through experiments and computational analyses. The results here provide insights that can be used to tailor the strengthening and toughening processes (the ECAE, heat treatment, etc.) of the AZ31 Mg alloy. The framework for establishing fracture toughness can also be applied to other metallic alloys such as Al alloys and steels.

Acknowledgements

This research is supported by the NSF Center for Computational Materials Design (CCMD) at Georgia Tech and Penn State. X. Guo acknowledges support from National Natural Science Foundation of China (Project No. 11102128). M. Zhou is also a WCU Professor in the School of Mechanical and Aerospace Engineering at Seoul National University and acknowledges support from the National Research Foundation of Korea through WCU Grant No. R31-2009-000-10083-0.

References

[1] Bettles CJ, Gibson MA. Current wrought magnesium alloys: strengths and weaknesses. JOM 2005;57:46–9.
[2] Duygulu O, Agnew SR. The effect of temperature and strain rate on the tensile properties of textured magnesium alloy AZ31B sheet. In: Kaplan H, editor. Magnesium technology. San Diego (CA): TMS; 2003. p. 237–42.
[3] Somekawa H, Mukai T. Effect of texture on fracture toughness in extruded AZ31 magnesium alloy. Scripta Mater 2005;53:541–5.
[4] Somekawa H, Mukai T. Fracture toughness in a rolled AZ31 magnesium alloy. J Alloy Compds 2006;417:209–13.
[5] Somekawa H, Mukai T. Fracture toughness in Mg–Al–Zn alloy processed by equal-channel-angular extrusion. Scripta Mater 2006;54:633–8.
[6] Kumar S, Curtin WA. Crack interaction with microstructure. Mater Today 2007;10:34–44.
[7] Song JH, Wang HW, Belytschko T. A comparative study on finite element methods for dynamic fracture. Comput Mech 2008;42:239–50.
[8] Needleman A. A continuum model for void nucleation by inclusion debonding. ASME J Appl Mech 1987;38:525–31.
[9] Camacho GT, Ortiz M. Computational modelling of impact damage in brittle materials. Int J Solids Struct 1996;33:2899–938.
[10] Xu XP, Needleman A. Numerical simulations of fast crack growth in brittle solids. J Mech Phys Solids 1994;42:1397–434.
[11] Siegmund T, Needleman A. A numerical study of dynamic crack growth in elastic-viscoplastic solids. Int J Solids Struct 1997;34:769–87.
[12] Miller O, Freund LB, Needleman A. Modeling and simulation of dynamic fragmentation in brittle materials. Int J Fract 1999;96:101–25.
[13] Needleman A. An analysis of decohesion along an imperfect interface. Int J Fract 1990;42:21–40.
[14] Xu XP, Needleman A. Numerical simulations of dynamic interfacial crack growth allowing for crack growth away from the bond line. Int J Fract 1995;74:253–75.
[15] Xu XP, Needleman A. Numerical simulations of dynamic crack growth along an interface. Int J Fract 1996;74:289–324.
[16] Tvergaard V, Hutchinson JW. The relation between crack growth and fracture process parameters in elastic-plastic solids. J Mech Phys Solids 1992;40:1377–97.

[17] Espinosa HD, Zavattieri PD. A grain level model for the study of failure initiation and evolution in polycrystalline brittle materials. Part I: theory and numerical implementation. Mech Mater 2003;35:333–64.
[18] Espinosa HD, Zavattieri PD. A grain level model for the study of failure initiation and evolution in polycrystalline brittle materials. Part II: numerical examples. Mech Mater 2003;35:365–94.
[19] Zavattieri PD, Espinosa HD. An examination of the competition between bulk behavior and interfacial behavior of ceramics subjected to dynamic pressure-shear loading. J Mech Phys Solids 2003;51:607–35.
[20] Zhai J, Zhou M. Finite element analysis of micromechanical failure modes in a heterogeneous ceramic material system. Int J Fract 2000;101:161–80.
[21] Zhai J, Tomar V, Zhou M. Micromechanical simulation of dynamic fracture using the cohesive finite element method. J Engng Mater Technol 2004;126:179–91.
[22] Tomar V, Zhai J, Zhou M. Bounds for element size in a variable stiffness cohesive finite element model. Int J Numer Methods Engng 2004;61:1894–920.
[23] Khan AS, Huang S. Continuum theory of plasticity. John Wiley & Sons; 1995.
[24] Johnson GR, Cook WH. A constitutive model and data for metals subjected to large strains, high strain rates and high temperatures. In: Proceedings of the 7th international symposium on Ballistics: The Hague, The Netherlands, 1983.
[25] Lou XY, Li M, Boger RK, Agnew SR, Wagoner RH. Hardening evolution of AZ31B Mg sheet. Int J Plast 2007;23:44–86.
[26] ABAQUS. ABAQUS theory manual and user's manual, version 6.7, Dassault; 2008.
[27] Anderson MP, Srolovitz DJ, Crest GS, Sahni PS. Computer simulation of grain growth – I. Kinetics. Acta Metall 1984;32:783–91.
[28] Weygand D, Brechet Y, Lepinoux J. A vertex dynamics simulation of grain growth in two dimensions. Philos Mag B 1998;78:329–52.
[29] Frost HJ, Thompson CV, Howe CL, Whang J. A two-dimensional computer simulation of capillarity-driven grain growth: preliminary results. Scripta Metal 1988;22:65–70.
[30] Telley H, Liebling TM, Mocellin A. The Laguerre model of grain growth in two dimensions I. Cellular structures viewed as dynamical Laguerre tessellations. Philos Mag B 1996;73:395–408.
[31] Geiger J, Roosz A, Barkoczy P. Simulation of grain coarsening in two dimensions by cellular-automaton. Acta Mater 2001;49:623–9.
[32] Chen LQ, Yang W. Computer simulation of the domain dynamics of a quenched system with a large number of nonconserved order parameters: the grain-growth kinetics. Phys Rev B 1994;50:15752–6.
[33] Steinbach I, Pezzolla F, Nestler B, Seeßelberg M, Prieler R, Schmitz GJ, et al. A phase field concept for multiphase systems. Physica D 1996;94:135–47.
[34] Fan D, Chen LQ. Computer simulation of grain growth using a continuum field model. Acta Mater 1997;45:611–22.
[35] Lusk MT. A phase-field paradigm for grain growth and recrystallization. Proc Roy Soc Lond A 1999;455:677–700.
[36] Lobkovsky AE, Warren JA. Phase-field model of crystal grains. J Cryst Growth 2001;225:282–8.
[37] Krill III CE, Chen LQ. Computer simulation of 3-D grain growth using a phase-field model. Acta Mater 2002;50:3057–73.
[38] Vedantam S, Patnaik BSV. Efficient numerical algorithm for multiphase field simulations. Phys Rev E 2006;73:016703.
[39] Vernerey F, Liu WK, Moran B, Olson G. Multi-length scale micromorphic process zone model. Comput Mech 2009;44:433–45.
[40] ASTM E399: standard test method for plane-strain fracture toughness of metallic materials. West Conshohocken (PA): American Society for Testing and Materials; 2001.
[41] Nakamura T, Wang Z. Simulations of crack propagation in porous materials. J Appl Mech 2001;68:242–51.
[42] Weng GJ. A homogenization scheme for the plastic properties of nanocrystalline materials. Rev Adv Mater Sci 2009;19:41–62.
[43] Capolungo L, Jochum C, Cherkaoui M, Qu J. Homogenization method for strength and inelastic behavior of nanocrystalline materials. Int J Plast 2005;21:67–82.
[44] Capolungo L, Cherkaoui M, Qu J. On the elastic–viscoplastic behavior of nanocrystalline materials. Int J Plast 2007;23:561–91.
[45] Anderson TL. Fracture mechanics: fundamentals and applications. 2nd ed. Boca Raton: CRC press; 1995.
[46] Dodds RH, Anderson TL, Kirk MT. A framework to correlate a/w ratio effects on elastic–plastic fracture-toughness (J_C). Int J Fract 1991;48:1–22.